Buckling failure analysis of storage tanks under the synergistic effects of fire and wind loads

Chen, Chao; Chen, Hang; Mo, Li; Xiao, Shenbin; Li, Changjun; Yang, Ming; Reniers, Genserik

DOI
10.1016/j.jlp.2023.105208

Publication date
2024

Document Version
Final published version

Published in
Journal of Loss Prevention in the Process Industries

Citation (APA)
Chen, C., Chen, H., Mo, L., Xiao, S., Li, C., Yang, M., & Reniers, G. (2024). Buckling failure analysis of storage tanks under the synergistic effects of fire and wind loads. *Journal of Loss Prevention in the Process Industries*, *87*, Article 105208. https://doi.org/10.1016/j.jlp.2023.105208

Journal of Loss Prevention in the Process Industries 87 (2024) 105208

Contents lists available at ScienceDirect

Journal of Loss Prevention in the Process Industries

journal homepage: www.elsevier.com/locate/jlp

Buckling failure analysis of storage tanks under the synergistic effects of fire and wind loads

Chao Chen [a,b,*], Hang Chen [c], Li Mo [c], Shenbin Xiao [c], Changjun Li [a], Ming Yang [d], Genserik Reniers [d,e,f]

[a] School of Petroleum Engineering, Southwest Petroleum University, Chengdu, 610500, China
[b] China Academy of Safety Science and Technology, Beijing, 100012, China
[c] School of Mechanical and Electrical Engineering, Southwest Petroleum University, Chengdu, 610500, China
[d] Safety and Security Science Group, Faculty of Technology, Policy and Management, TU Delft, Delft, the Netherlands
[e] Faculty of Applied Economics, Antwerp Research Group on Safety and Security (ARGoSS), University Antwerp, Antwerp, Belgium
[f] CEDON, KULeuven, Campus Brussels, Brussels, Belgium

ARTICLE INFO

Keywords:
Thermal post-buckling
Wind load
Storage tank
Numerical simulation
Domino effects

ABSTRACT

Fire-induced domino effect is one of the main threats to hazardous material storage tanks, and many attempts have been conducted to assess the vulnerability of storage tanks exposed to fire to evaluate domino effect risk. However, past research ignored the influence of wind load on the thermal buckling behavior of storage tanks exposed to fire, which may underestimate the risk of exposed tanks. This paper thus conducts a numerical simulation of the thermal buckling behavior of steel vertical dome storage tanks under the synergistic effect of static wind loads and thermal effects. The effects of wind parameters and heat radiation parameters on the thermal post-buckling behavior and the time to failure (*ttf*) of storage tanks are investigated to analyze the synergistic effects of fire and wind loads. By comparing the circumferential and meridional stresses before and after the thermal post-buckling stage, it is found that under the disturbing effect of the positive wind pressure load, the thermal post-buckling of the tanks on downwind occurs earlier and more severe. Besides, the effects of wind angle, fire location height, and diameter on buckling damage were investigated. The comparative analysis of different scenarios shows that the tanks in the windy scenario are more prone to thermal post-buckling, and the deformation is intensified, with an increased likelihood of failure.

1. Introduction

The process industry plays an important role in sustaining daily life and promoting global economic development by supporting fuels, chemical products, and raw materials. With the expansion of the product demand of the process industry, many storage tanks are located together for storing hazardous materials such as gasoline, liquid natural gas (LNG), and benzene (Paltrinieri et al., 2009). Once a fire occurs at a storage tank, domino effects may be triggered due to the heat radiation induced by the primary fire and the vulnerability of storage tanks exposed to fire, resulting in the overall losses being more severe than the primary event (Landucci et al., 2009; Reniers and Cozzani, 2013; Chen et al., 2020).

Fire is the most common accident scenario in domino effect accidents, responsible for 52.4% of domino effects in the process industry (Darbra et al., 2010; He et al., 2022). Fire-induced domino effects always occurred in oil storage tank farms, such as the ITC company fire accident in 2019, in Houston, the US (Chen et al., 2020; Lan et al., 2022). In domino effects, there are complex escalation mechanisms or interdependencies that are challenging to risk management (Necci et al., 2015; Jiang et al., 2019; Ding et al., 2021; Li et al., 2023b; Chen et al., 2021). In storage tank farms, most fires initially originate in one tank, and then heat is transferred to the surrounding area through thermal radiation. Fire may damage the surrounding facilities in a short time (time to failure), leading to a secondary fire or explosion (Landucci et al., 2009; Zhang et al., 2019; Li et al., 2023a; Malik et al., 2023). Compared to the windless situation, the flame is tilted by the wind, and the temperature rise of the tank located downwind is accelerated, resulting in a shorter failure time. In the case of strong thermal radiation and thermal shock, a storage tank, as a typical thin-walled structure, is highly likely

---

* Corresponding author. School of Petroleum Engineering, Southwest Petroleum University, Chengdu, 610500, China.
E-mail address: chenchaoswpu@gmail.com (C. Chen).

https://doi.org/10.1016/j.jlp.2023.105208
Received 31 August 2022; Received in revised form 22 October 2023; Accepted 3 November 2023

to collapse due to local buckling, thus triggering a chain accident and causing the escalation and expansion of the fire (Godoy, 2016; Chen et al., 2020; Dong et al., 2020). Therefore, many attempts have been made to investigate the thermal buckling of storage tanks to predict the time to failure (*ttf*) which is a key parameter for risk assessment of domino effects (Landucci et al., 2009).

Studies on the thermal buckling of storage tanks exposed to heat radiation have been conducted in recent decades. Liu (2011) studied the thermal buckling mechanism of storage tanks inspired by the Buncefield oil depot fire accident and presented a simplified temperature field distribution model of the tanks exposed to fire. Subsequently, a correlation between the spread of tank fires and the thermodynamics of storage tanks was developed (Reniers and Cozzani, 2013). Batista-Abreu and Godoy (2013) studied the thermal buckling behavior of open-topped storage tanks and demonstrated that the geometry of the tanks will undergo abrupt changes to balance the internal stress changes during warming, and the empty tanks are the lower limit of their structural stability. Pantousa (2018) conducted a numerical study on the thermal buckling of empty storage tanks under multiple pool fire scenarios. The results show that the critical time when the tank fails increases with increasing burning tanks. Pantousa et al. (2018) investigated the thermal buckling behavior of unstiffened and stiffened fixed-roof tanks under non-uniform heating and demonstrated that using a horizontal ring stiffening method can enhance the inherent fire resistance of tanks. Li et al. (2019) studied the thermal buckling behavior of storage tanks under different environmental scenarios by considering the pulsation effect of flames. Besides, they also investigated the thermal buckling behavior of tanks under the combined effects of debris impact and thermal radiation and discussed the effect of combined loads on the failure mode of tanks (Li et al., 2021). Jaca et al. (2021) demonstrated differences in the equilibrium paths of thermal post-buckling in tanks due to differences in their temperatures at different wind speeds. These studies show that storage tanks located in high-temperature environments undergo thermal buckling due to the combined effect of their boundary condition constraints and non-uniform thermal expansion. The thermal buckling behavior depends on the temperature field distribution and load distribution of the storage tank.

Flames are influenced by environmental factors and exhibit different combustion characteristics; thus, past research also considers the effects of environmental factors on the temperature field distribution of surrounding objects. Previous studies show that solid flame models can appropriately represent the flame properties of storage tanks in different environments by comparing the model results with experiments (Mansour, 2012; Santos and Landesmann, 2014; Espinosa et al., 2019). In a solid two-layer flame model, the flame can be divided into a region with a bright flame at the bottom and a dark flame region with thick smoke at the top. Each part has a different thermal radiation capacity and height (Drysdale, 2011). In windless conditions, the flame is a vertical cylinder, and when subjected to wind, the cross-sectional shape of the flame changes to an ellipse, and the column is tilted (Mudan, 1984). For tank farms where petrochemicals are stored, the model is applicable for all fuel types. In addition, it has the advantage of being a simple model, less computationally intensive, and more effective in measuring thermal radiation from distant targets compared to computational fluid dynamics models (Rew et al., 1997).

Besides thermal buckling, many studies also consider the bucking of storage tanks caused by wind since the windward side of the tank is subjected to positive pressure, and the rest of the tank is subjected to negative pressure. Considering wind loads alone, the difference in the wind load between the windward and leeward sides of the tank and the possibility of buckling increases with increasing wind speed (Godoy, 2016). For the wind pressure distribution law on the surface of the object, the corresponding functional expressions are obtained mainly by wind tunnel tests on similar models, followed by numerical fitting of the test data. Godoy (2007) demonstrated that the extent to which wind buckling of tanks occurs is related to their filling state. Maraveas et al. (2015) numerically evaluated the wind buckling of open tanks based on the wind pressure distribution expression in different design codes and found deficiencies in the current design codes. The buckling behavior of storage tanks is controlled by the positive pressure on the windward side, while the wind pressure in other areas has almost no influence (Zhao and Lin, 2014). Numerical studies indicate that fixed-top tanks have a stronger resistance to wind buckling than open tanks (Portela and Godoy, 2005a, 2005b; Uematsu et al., 2018).

In a coupled wind-fire scenario, a tank located not only has an altered rate of warming but also be subjected to non-uniform wind loads. However, past studies did not consider the additional wind loads on the storage tanks. Therefore, when the wind speed increases to a certain level, under the synergistic effects of wind load and flame, the thermal buckling behavior of the storage tank may change, leading to changes in the time to failure. The neglect of wind load in thermal buckling may underestimate the domino effect risk, resulting in unreasonable safety management and unpredicted losses. Besides, the difference in tank heights between the fire source tank and the exposed tank is not considered in past failure studies. Therefore, this study conducts a numerical study to analyze the thermal buckling behavior of storage tanks under the synergistic effects of wind and fire, considering the influence of tank heights. In the numerical model, the temperature distribution of vertical domed storage tanks under different wind speeds is first studied based on a solid flame model to get the variation law of wind speed and temperature. Then, the critical buckling load factor is obtained by applying wind load to the tank based on the wind pressure distribution law function. Besides, the thermal buckling behavior of the tank under different wind parameters is studied to analyze the stress redistribution when thermal post-buckling occurs. Finally, the effects of different wind angles, fire source tank heights, and diameters on the thermal post-buckling behavior of storage tanks are investigated to support the prediction of tank failure and the calculation of *ttf*, risk assessment of the domino effect triggered by fire, and the inherent design of storage tank areas.

2. Numerical modeling

Buckling damage analysis of storage tanks under the synergistic effect of fire and wind loads requires heat radiation modeling, wind load modeling, and bucking modeling. Both the temperature field obtained in the heat radiation modeling and the wind loads obtained in wind load modeling are used in the buckling analysis. The finite element analysis software Abaqus is adopted to implement buckling analysis since it has powerful nonlinear solving capability and can obtain the coupling analysis of different physical fields. The buckling analysis of storage tanks under the synergistic effect of wind and fire involves not only thermal coupling but also nonlinear deformation, therefore, Abaqus is used to carry out the numerical study.

2.1. Heat radiation modeling

In fire modeling in thermal buckling studies of storage tanks, the source of the fire at the top of a storage tank is called the source tank, and the flame of the fire transfers heat in all directions through heat radiation. The target tank is the adjacent storage tank exposed to heat radiation. The main parameters describing the geometric characteristics of the flame are the cross-sectional shape, the flame diameter D_f (D'_f), the flame length L_f and the flame tilt angle φ, as shown in Fig. 1.

In the absence of wind, the flame diameter D_f is equal to the diameter of the source tank. Wind causes the flame to move laterally at a certain distance, resulting in the cross-sectional shape becoming an elliptical tangent to the circle, and the long axis is recorded as D'_f. The flame length L_f can be calculated based on Eqs. (1) and (2) (Thomas, 1963) in the windless and windy states, respectively.

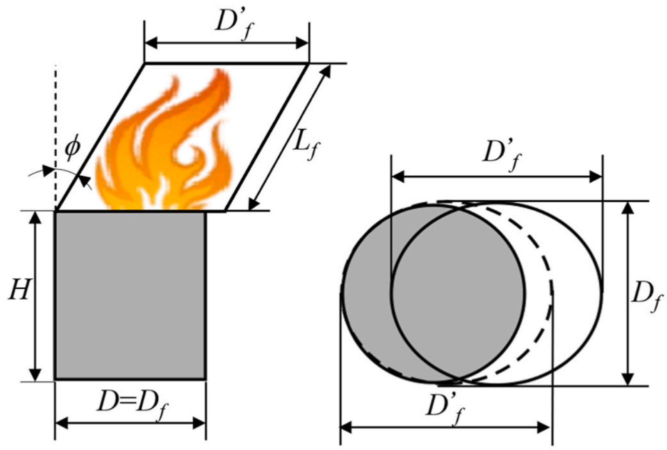

Fig. 1. Wind-affected flame model.

$$L_f= 42D_f\cdot(m^*)^{0.61} \tag{1}$$

$$L_f= 55D_f\cdot(m^*)^{2/3}\cdot(u^*)^{-0.21} \tag{2}$$

where L_f is the overall length of the flame (m), D_f is the flame diameter (m), and u^* is the non-dimensional wind speed. m^* is the non-dimensional mass burning rate of the fuel, and it can be obtained by using Eqs. (3) and (4) (Hurley et al., 2015):

$$m^* = m_b \Big/ \left[\rho\cdot(gD_f)^{0.5}\right] \tag{3}$$

$$m_b = m_{\max}\left(1-e^{-k_\beta D_f}\right) \tag{4}$$

Where g is the acceleration due to gravity (m/s^2), ρ is the air density (kg/m^3), m_b is the mass combustion rate of the fuel (kg/m^{2}s), $m_{\max}$ is the maximum combustion rate of the fuel (kg/m^{2}s), and k_β is the fuel experience coefficient. For gasoline fuel, $m_{\max} = 0.055$ kg/m^{2}s, $k_\beta = 2.1$.

The length of the bright flame region can be calculated according to Eq. (5) (Espinosa et al., 2019):

$$L_1 = 11.404(m^*)^{1.13}(u^*)^{0.179}\left(\frac{N_c}{N_H}\right)^{-2.49}D_f \tag{5}$$

where L_1 is the length of the bright flame part of the flame (m), the total length of the bright flame and the dark flame is represented by L_f. N_C and N_H are the number of carbon and hydrogen atoms in the fuel.

According to the study on fire hazards (Beyler, 2016), the flame inclination angle φ is related to u^* and can be calculated using Eqs. (6) and (7) as follows:

$$u^* = \frac{u_\infty}{\left(D_f\frac{gm_b}{\rho}\right)^{1/3}} \tag{6}$$

$$\cos\varphi = \begin{cases} \dfrac{1}{\sqrt{\boldsymbol{u}^*}}, \boldsymbol{u}^* \geq 1 \\ 1, \boldsymbol{u}^* < 1 \end{cases} \tag{7}$$

where φ is the deflection angle of the flame (°), and u_∞ is the free field wind speed (m/s). The cross-sectional shape of the flame changes when it moves under the effect of wind. The long axis D'_f can be calculated according to Eq. (8). F_r is the non-dimensional Froude number which is related to u_∞, as shown in Eq. (9) (Hurley et al., 2015).

$$D_f^{'}= 1.5D_f\cdot F_r^{0.069} \tag{8}$$

$$F_r = \frac{{u_\infty}^2}{gD_f} \tag{9}$$

For gasoline, the maximum experimental emitted power $E_{\max}$ ranges from 120 to 170 kW/m^2 in the bright flame region and about 20 kW/m^2 in the dark flame E_{soot} (Espinosa et al., 2019). However, with increasing the flame diameter, the glowing area of the flame decreases, the flame surface becomes mostly covered with smoke, and the glowing area becomes blurred (Muñoz et al., 2007). When $D = 20$ m, the entire flame surface will be covered with smoke, and the average emitted power by the flame is approximately equal to the power emitted by the smoke (Muñoz et al., 2007).

In the statistics of flame heat radiation for various types of fuels and pool fire sizes, the overall thermal radiation power of the flame is 150–220 kW/m^2 when the diameter of the liquid hydrocarbon type pool fire is 20 m (Mudan, 1984). However, the use of an overall average emitted power to express the radiative power of the flame would result in a small emitted power in local areas (Beyler, 2016). Therefore, for the solid double-layer flame model with gasoline as fuel, the average emitted power $E_{av\text{-}max}$ in the bright flame region considers the effect of smoke and is calculated from Eq. (10):

$$E_{\text{av}-\max} = E_{\max}\,Exp\left(-0.12D_f\right) + E_{soot}\left[1 - Exp\left(-0.12D_f\right)\right] \tag{10}$$

where the emitted power of the bright flame $E_{\max} = 140$ kW/m^2 and the dark flame $E_{soot} = 20$ kW/m^2. The correlation between the equivalent temperature of each region of the flame surface and the average emitted power E_{av} (Santos and Landesmann, 2014) is shown in Eq. (11) (Santos and Landesmann, 2014):

$$T_{fe} = \sqrt[4]{\frac{\varepsilon\sigma T_a^4 + E_{av}\tau}{\varepsilon\sigma}} \tag{11}$$

where T_{fe} (°C) represents the equivalent temperature of the flame surface, E_{av} is equal to $E_{av\text{-}max}$ for the bright flame, and E_{soot} for the dark flame. ε is the emissivity of the flame and takes the value of 1. σ is the Stefan-Boltzmann constant (5.67×10^{-8}W/m^2/K^4). τ is the atmospheric transmittance, calculated by Eq. (12) (Santos and Landesmann, 2014):

$$\tau = \begin{cases} 0.976(d)^{-0.06}, d < 5m \\ 1.029(d)^{-0.09}, 5 \leq d \leq 55m \\ 1.159(d)^{-0.12}, d > 55m \end{cases} \tag{12}$$

Fig. 2(a–b) shows the simplified model of the target tank and the top view of the model considering the wind direction. The distance between the two tanks is d, and the wind angle γ is the angle between the wind direction and the line connecting the centers of the two tanks. The target tank is selected according to the actual engineering requirements (API, 2007; (GB50341, 2014)), with a diameter of 20 m and a tank height of 17.82 m. The wall thickness t of each course is shown in Table 1, and the three-dimensional model is shown in Fig. 2. Besides, the diameter of the source tank is denoted as D, which is identical to the diameter of the target tank, and the height is denoted as H.

The average convective heat transfer coefficient $\overline{h_c}(W/m^2\cdot K)$ on the external surface of the target tank can be calculated according to Rebec et al. (2014):

$$\overline{h_c} = N_u K_a / L^* \tag{13}$$

where N_u is the Nusselt number, K_a is the thermal conductivity of air (W/m·K), and L^* is the characteristic length (m). For laminar flow and turbulent flow, the Nusselt number can be calculated by Eqs. (14) and (15), respectively (Rebec et al., 2014).

$$N_u= 0.664R_e^{\frac{1}{2}}P_r^{\frac{1}{3}} \tag{14}$$

$$N_u = \left(0.037R_e^{\frac{4}{5}} - 871\right)P_r^{\frac{1}{3}} \tag{15}$$

where P_r is the Prandtl number, equal to 0.72 for air in laminar and turbulent conditions; Re is the Reynolds number, calculated by Eq. (16):

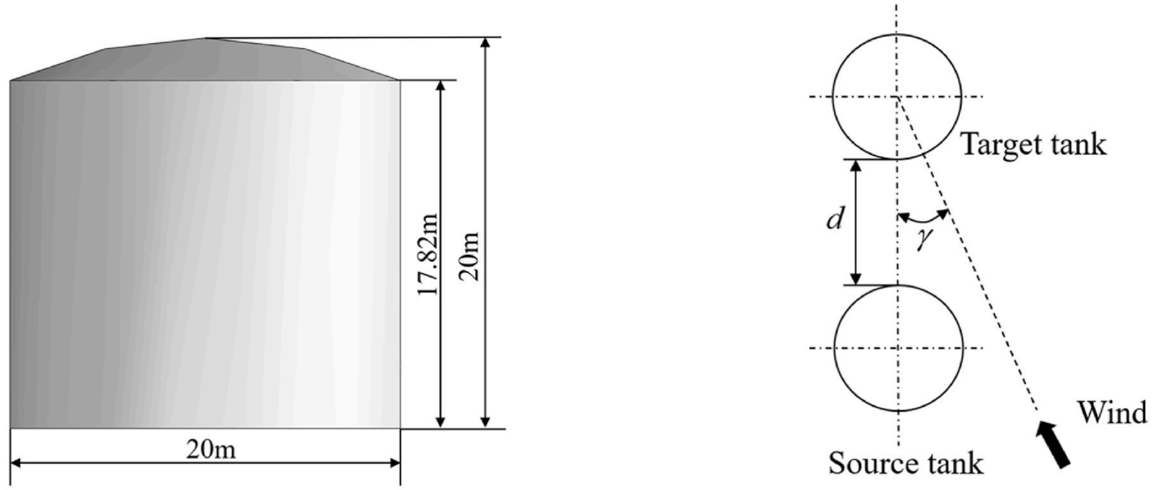

(a) Simplified model of target tank

(b) Top view of storage tank

Fig. 2. Simplified model of storage tank.

Table 1
Structural parameters of the target tank (Hu, 2016).

Name	Thickness (mm)	Height (m)
1st shell course	13	1.78
2nd shell course	12	1.78
3rd shell course	11	1.78
4th shell course	10	1.78
5th shell course	9	1.78
6th shell course	7	1.78
7th to 9th shell course	6	1.78
10th shell course	6	1.8
Dome	5	–

$$Re = u_\infty L^* / v \tag{16}$$

where ν is the kinematic viscosity of air (m^2/s). If $Re < 10^5$, it is regarded as laminar flow, and the wind speed is turbulent except for the free field wind speed $u_\infty = 0$. For no wind condition, $u_\infty = 0.1$ m/s is taken into the calculation.

To consider the lower limit of structural stability of the storage tank, the target tank in this paper is an empty tank, which is the worst case for its structural stability under heat radiation effects or wind loads (Liu, 2011; Maraveas et al., 2015; Pantousa et al., 2018). Moreover, in exothermic combustion, only the surface layer of fuel is involved, and the temperature change of the fuel at the depth is not obvious (Li et al., 2021). It is assumed that the initial temperature of the source tank and the environment are identical, and the value is taken as 20 °C.

The material of the tank is Q345, the emissivity of the outer surface is 0.8, and the emissivity of the inner surface is 0.3. The physical-mechanical properties of Q345 are a function of temperature (Li et al., 2019). Table 2 lists the constant pressure specific heat c_p, thermal conductivity k, coefficient of thermal expansion α, modulus of elasticity E, and Poisson's ratio μ of Q345 at different temperatures T. The stress-strain curve of the material at high temperatures can be obtained in the literature (Li et al., 2021). Besides, the density of 7850 kg/m^3 does not change with temperature.

Table 2
Thermo-physical properties of Q345 (Dong and Yuan, 2000).

T (°C)	c_p (J/kg/K)	k (W/m/K)	$\alpha \times 10^6$ (1/°C)	E (GPa)	μ
20	460	53.2	–	206	0.3
100	481	51.1	8.31	201	
200	523	47.7	10.99	189	
300	557	44	12.31	181	
400	607	39.6	13.22	172	
500	673	36	13.71	162	
600	–	–	13.94	152	

The finite element model of the tank and flame in the 5 m/s wind speed scenario is shown in Fig. 3. In the thermal radiation analysis stage, transient thermal analysis was used to solve the temperature field distribution of the target tank. The models are all built using shell units, and the selected unit type is DS4, which is a four-node heat transfer quadrilateral shell with a wide range of applications (Liu, 2011). Grid-independent validation is required to ensure the accuracy of the computational results and the effective allocation of computational resources. In this paper, there is experimental analysis, when the number of meshes is 22398, it can ensure the accuracy of the calculation. Among them, the number of meshing of the target tank in the circumferential direction is 128, and the number of axial directions of the tank is 76.

2.2. Wind load modeling

The flame is tilted under the influence of the wind, the radiation capacity of the flame and the heat dissipation coefficient of the airflow depend on the wind, and the temperature field distribution of the target tank is also changed with the wind. The heat radiation modeling in Section 2.1 is only used to solve the temperature field distribution, ignoring the role of the wind load on the tank, and only considering the wind to make the flame skewed (from Eq. (7) to calculate the degree of flame tilt). The wind load modeling in this section is applied in the

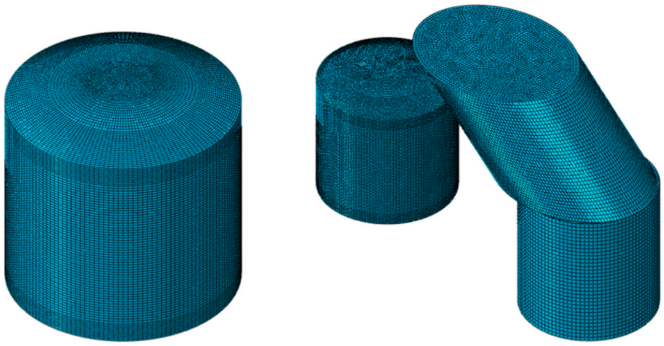

Fig. 3. Meshing of finite element models.

thermal buckling analysis.

The wind load is divided into static wind load and pulsating wind load, which belongs to the variable load of the building structure load. For buildings with a height not exceeding 30 m and a height-to-width ratio not greater than 3/2, the effect of pulsating wind can be ignored (GB50009, 2012). Therefore, the wind load on the storage tank in this paper is regarded as a static wind load, and the expression for the wind pressure amplitude is as follows (GB50009, 2012):

$$\begin{cases} w_k = \beta_z \mu_s \mu_z w_0 \\ w_0 = u_\infty^2 / 1.6 \end{cases} \tag{17}$$

where w_k is the wind pressure amplitude (Pa); β_z is the wind vibration coefficient at a height of Z (m) from the ground, taken as 1 in this paper. μ_s and μ_z denote the wind load shape coefficient and wind pressure height variation coefficient, respectively. w_0 is the basic wind pressure (Pa), which should be selected once every 100 years (Lin et al., 2010; GB/T 20368, 2006).

The circumferential and vertical wind pressure distribution of the tank are variables. The wind pressure in the vertical direction can be calculated based on Eq. (17), and the distribution of vertical wind pressure and the wind pressure in the area of the tank dome is shown in Fig. 4. Among them, the distribution of vertical wind pressure is related to the height and topography, mainly involving μ_s and μ_z. For terrain features of class B, μ_z can be calculated by Eq. (18) (Jin and Zhao, 2012; GB50009, 2012):

$$\mu_z = \begin{cases} 1, Z \leq 10\text{m} \\ 1.1 \times 10^{-6} Z^3 - 2.7 \times 10^{-4} Z^2 + 0.028Z + 0.76, 10 < Z \leq 100\text{m} \\ 1.7 \times 10^{-8} Z^3 - 1.7 \times 10^{-5} Z^2 + 0.0086Z + 1.3, 100 < Z \leq 350\text{m} \\ 2.91, Z > 350\text{m} \end{cases} \tag{18}$$

The wind pressure distribution in the tank dome area is calculated according to Eq. (19):

$$\mu_s = -\cos^2 \varphi \tag{19}$$

In the study of circumferential wind pressure distribution of cylindrical buildings, the Fourier series is commonly used to carry out calculations, as shown in Eq. (20) (Maraveas et al., 2015).

$$P = \lambda \sum_{i=0}^{7} c_i \cos(i\theta) \tag{20}$$

where P is the wind pressure (Pa); λ is the load amplification factor; θ is the angle along the circumferential direction; c_i is the Fourier coefficient. Eq. (20) is widely used in the study of wind buckling of cylindrical thin-walled storage tanks. The values of c_i given by (Rish and FOURIER, 1967) and ACI-ASCE are adopted in this study. Besides, concerning the body shape coefficients for the circumferential distribution of cylindrical buildings, this study uses a series of discrete values for different angles (ACI-ASCE Committee 334, 1976; GB50009, 2012).

A comparison of different values of coefficients is shown in Fig. 4. It can be found that the wind load is symmetrically distributed over the storage tank. Although the change trends of the three curves are identical, it will be safer to adopt the criteria in the load specification. Therefore, this paper calculates the circumferential wind load body shape coefficient of the storage tank through data fitting of discrete values.

Based on the above wind load model, the amplitude of the wind load on each region of the storage tank in a windy environment can be calculated. The thermal buckling stage is a generic static analysis step and the cell type of the model is the S4R shell cell (Li et al., 2021). The S4R is a general-purpose shell unit type that utilizes a reduced integration method and includes hourglass mode control for stable performance. Then gravity and wind loads are applied to the tank as a whole, where the application of wind loads is obtained by creating a column coordinate system in Abaqus to set up the revolving field. As shown in Fig. 5, the purple arrows represent wind loads and the yellow arrows represent gravity.

2.3. Buckling modeling

Riks is an effective method for calculating the post-buckling state when the tank is loaded by only external forces. However, when thermal effects are involved, Riks is proven to be no longer reliable, and the artificial damping method (ADM) is considered the best method to solve the thermal buckling problem of storage tanks (Liu, 2011; Pantousa and Godoy, 2019). ADM can capture the thermal post-buckling state of the storage tank and has been used and validated by many authors (Batista-Abreu and Godoy, 2013; Uematsu et al., 2018). When considering the total external load P and internal force Q of the structure in ADM, artificial damping force F_D is also introduced to establish a balance of the three, as shown in the following formula:

$$P - Q - F_D = 0 \tag{21}$$

$$F_D = c \times M^* \times v \tag{22}$$

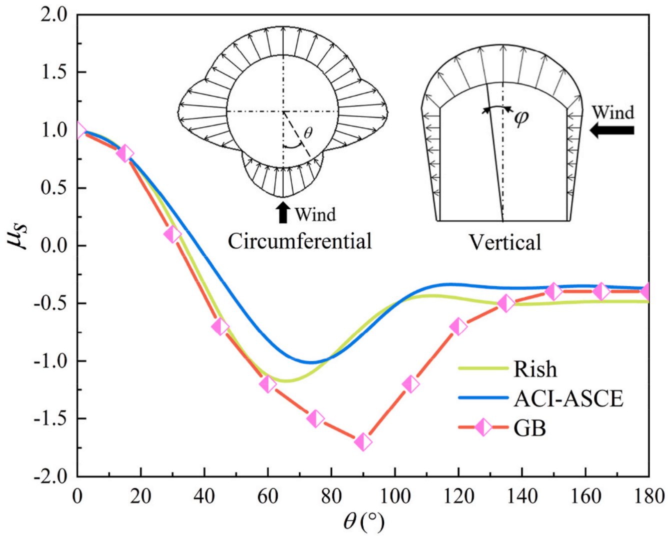

Fig. 4. Comparison of body shape coefficients.

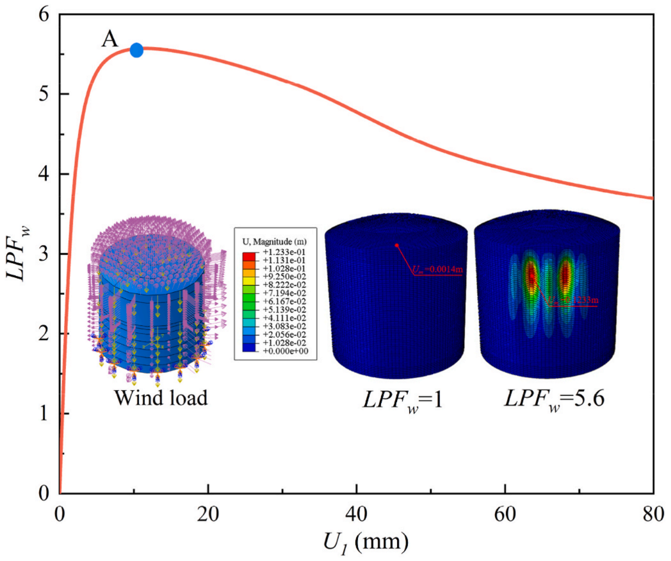

Fig. 5. Load-displacement curve under wind load.

where M^* is the artificial mass matrix of unit density, υ is the velocity vector of the node, and c is the damping ratio. The damping ratio c is the ratio of the viscous damping dissipation energy (ALLSD) to the total strain energy (ALLIE).

When the model is stabilized, the viscous damping dissipation energy is negligible compared to the total strain energy of the structural system and the additional damping (F_D) does not affect the structural performance. If the local region of the structure becomes unstable, the local velocity increases and some of the strain energy released is dissipated by the applied damping (F_D) to help the structure pass through the local instability without terminating due to convergence difficulties (Liu, 2011). In Abaqus, the damping ratio c can be automatically updated based on the convergence conditions and the input initial dissipated energy fraction (default 0.0002).

An experimental analysis is required to determine the input value of the initial dissipated energy fraction. With decreasing the input value, the critical buckling temperature of the tank will eventually converge to a stable value (Godoy and Batista-Abreu, 2012; Pantousa, 2018). In terms of different studied scenarios in this paper, it is determined through experimental analysis. The critical buckling temperature converges when the input value of the initial dissipated energy fraction is in the interval of 5×10^{-8} to 5×10^{-9}.

3. Modeling results

On the windward side, the storage tank is subject to positive pressure, and the rest of the surface is subject to negative pressure. The loads of the tank are non-uniformly distributed. Cases of buckling of empty or low-filled storage tanks subjected to external non-uniform wind loads occur from time to time. The type of buckling of storage tanks needs to be explored before carrying out a numerical study on the thermal buckling behavior of storage tanks in wind-fire coupling.

3.1. Buckling analysis under wind load

Based on the description in Section 2.2, a maximum wind speed of 25 m/s can be taken for Chengdu, China, and then the wind load is applied to the storage tank. Based on the nonlinear large deformation theory, the classical buckling mode is introduced as the initial defect and then the Riks method is used to analyze the buckling of the tank under the wind load alone to obtain the wind load scaling factor LPF_w, and the whole process of wind buckling response (Maraveas et al., 2015). Taking the maximum deformation point of the tank as a reference, the load-displacement curves of radial displacement U_1 and LPF_w at this point are shown in Fig. 5, U_m is the maximum deformation of the tank.

For better visualization, the scale factor of the view in the text is chosen to be 10. According to the load-displacement curve, the deformation of the tank at full loading ($LPF_w = 1$) and critical buckling ($LPF_w = 5.6$), it is known that LPF_w tends to linearly increase until the wind load increases to point A ($LPF_w = 5.6$). After point A, U_1 increases rapidly, the buckling instability of the storage tank occurs, and the maximum deformation occurs in the windward area. When $LPF_w = 5.6$, it corresponds to wind speed $u_\infty = 59.2$ m/s and wind class $W_c = 17$, a hurricane. The wind speed in Chengdu is almost impossible to reach this level, so the type of buckling of the tanks in this paper belongs to thermal buckling and it is no need to consider the buckling condition under the effect of wind load alone.

3.2. Buckling analysis of wind-fire synergies

The analysis in Section 3.1 shows that only thermal effects cause the buckling of the tanks studied in this paper. The wind load only affects the degree of deformation of the tank and the *ttf*. To better compare the effect of wind loads on the thermal buckling behavior of storage tanks, the shielding effect of wind loads by adjacent buildings and facilities is ignored in the subsequent elements of the study, i.e., extreme conditions are considered.

The whole process of the thermal buckling phenomenon for storage tanks can be divided into two stages: in the thermal pre-buckling stage, linear thermal expansion occurs in the target tank; as the warming process continues, the variability of the temperature between regions is revealed; due to the non-uniform confined thermal expansion and the degradation of the mechanical properties of the material, the target tank undergoes thermal post-buckling, with folds appearing in the weak part of the tank, followed by a large non-linear deformation.

Fig. 6 plots the evolution of the damping ratio with time for a scenario with a wind speed of 25 m/s, with and without wind load (W25) applied, and T_{end} denotes the 3600th s of the target tank warming process. When thermal post-buckling has not occurred, the viscous damping dissipation energy accounts for a very small proportion of the total strain energy, and the damping ratio tends to zero. With the continuation of the heating process, the difference in thermal expansion of different parts of the tank increases, and the damping ratio rapidly increases near *ttf*, which predicts the appearance of thermal post-buckling.

At the onset of the thermal post-buckling stage, the upper region of the tank is transformed from an initial state of thermal expansion to the appearance of folds, and then the fold deformation is rapidly transformed into a concave deformation within a short time. The damping ratio tends to decrease in the interval from *ttf* to Tend, indicating that the tank achieves a relatively stable equilibrium of the structure.

It is worth noting that during the thermal post-buckling phase, the structural behavior of the tank is unstable and undergoes different stages of buckling. The first thermal post-buckling time of the tank is considered as the time to failure *ttf*, and the corresponding temperature is denoted as the critical buckling temperature T_L. Comparing W25 and NW25, the thermal post-buckling behavior occurs 85 s earlier after applying the wind load to each region of the tank. The earlier occurrence of the thermal post-buckling behavior of the tank predicts the decrease of *ttf* and the decrease of the structural stability. In the same time interval, due to the early reduction of structural stability, the possibility of subsequent reoccurrence of buckling increases, and the deformation and load-carrying performance of the tank will further deteriorate.

4. Parameter analysis

4.1. Effects of wind speeds

Taking the source tank height $H = 20$ m and the spacing $d = 20$ m, the thermal buckling behavior of the target tank under different wind speeds is investigated using the developed numerical model. The results

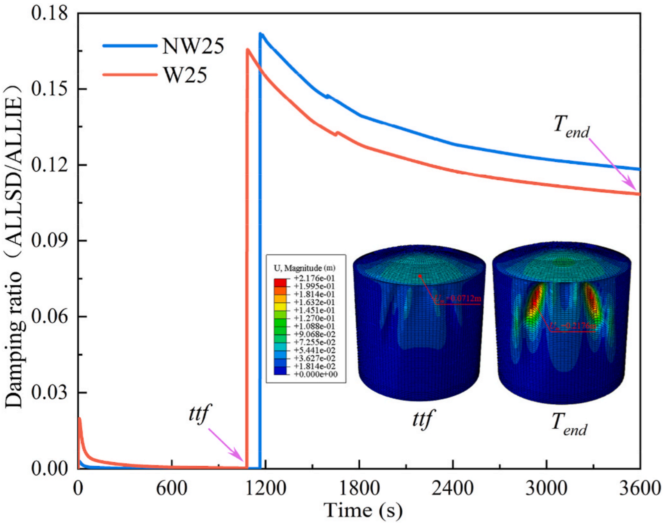

Fig. 6. Evolution of the damping ratio over time.

show a significant difference in the temperature distribution in each region of the tank under different wind speeds. The tank can be divided into a high-temperature region facing the flame and a low-temperature region at the back. With the increase in wind speed, the hot areas gradually converge towards the tank dome. As the flame tilt increases, the hot area at the tank dome also expands along the top edge and slowly around.

The temperature distribution in the various regions of the tank considerably varies and can be divided into a high-temperature region facing the flame and a low-temperature region at the back. As the wind speed increases, the high-temperature region gradually converges towards the top region of the tank. The high-temperature region at the top of the tank also slowly expands along the top edge to the surrounding area due to the increasing inclination of the flame. In the initial stage of a fire, the heating rate of the tank is directly proportional to the wind speed. However, when the wind speed further increases, the convective heat dissipation of air begins to gradually dominate and the warming rate decreases. The maximum temperature (T_H) of the target tank first increases and then decreases in different wind speed scenarios because the convective heat dissipation coefficient increases with the increase in wind speed.

The non-uniform thermal expansion under boundary condition constraints is an important reason for the thermal post-buckling of storage tanks. When the flame is tilted to different degrees, the heating rate of the storage tank increases significantly. Compared with the no-wind scenario, the wind-affected storage tank can reach the thermal stabilization state earlier, so the T_L and T_H show the same change trend under different wind speeds, and the difference between them is small. Therefore, wind load has little effect on T_L while mainly has an impact on *ttf*.

4.1.1. Stress redistributions at buckling

The variation of *ttf* in different wind speed scenarios is shown in Fig. 7. Due to the effect of wind on the rate of warming, the presence of wind causes a significant decrease in *ttf* compared to the scenario with zero wind speed. Considering the effect of wind load, there is a difference in *ttf* at the same wind speed, and this difference increases with the increase of wind speed. Besides, the point of maximum deformation of the tank is located in the windward positive pressure zone. The path through this point along the circumferential direction of the tank is recorded as path 1, and the path along the meridional direction from the bottom to the tank dome is recorded as path 2.

In the case where wind loads are not considered, there is variability in the distribution of temperature on the surface of the tank, resulting in uneven thermal expansion of the tank wall. Besides, constraints from the tank dome, the bottom of the tank, and the cryogenic zone generate bending moments at the top and bottom of the tank, so thermal post-buckling first occurs at the upper part of the tank wall in which the wall thickness is weak.

The comparison of Fig. 8(a–c) at the time *ttf* shows that when the wind load is applied on path 1, the radial displacement undulates more drastically and the degree of folds increases, making the alternating changes of circumferential and meridional stresses more frequent. The results demonstrate that even if wind loads are not considered, the tank is subject to its constraints and non-uniform thermal expansion in the region can generate folds. When wind load is considered, this area in the windward pressure zone can only affect but not change the form of deformation on a large scale, so the degree of folding increases. At the time T_{end}, the tank is subject to thermal post-buckling and the inward depression becomes the dominant deformation feature. Besides, the circumferential and meridional stresses increase due to the increase in the degree of depression deformation when the wind load is applied.

As shown in Fig. 8(d–f), it can be known that the meridional stress on path 2 is smaller at the time *ttf* than that of the wind load when it is not applied. This is because the thermal expansion of the tank is reduced after being subjected to wind load. The inward depression deformation occurs in advance due to the imminent thermal post-buckling at this time and the disturbance of wind load in some areas of the tank. In terms of the trend of the radial displacement of the tank, the radial displacement to the outside decreases by applying the wind load. Combined with Fig. 6, it can be seen that the degree of fold deformation increases from the bottom up along the tank. As mentioned before, the degree of creasing increases with the wind, so the circumferential stress along path 2 increases with wind loads.

At the time T_{end} of path 2, the tank is subjected to thermal post-buckling, and the depression formed inward becomes the most dominant deformation feature of the tank. After being subjected to wind load, the degree of inward depression deformation increases, so the amplitude of circumferential and meridional stresses increases. The degree of deformation of the tank dome bulging outward increases again at this time, and the degree of deformation is more significant by applying the wind load. Therefore, for the tank with applied wind load, the degree of depression deformation near the upper part region of the tank wall is reduced, so the circumferential stress amplitude decreases. In the meridional direction, the constraint from the tank dome in this region is again weakened, and the amplitude of the meridional stress is reduced.

In path 2, three different regions can be divided: the tank dome, the equal wall thickness region in layers 7 to 10, and the lower non-uniform wall thickness region. There are abrupt changes in stress amplitude at both the wall thickness and the intersection of the regions, with the most pronounced changes in the meridional stress, as shown in the section of the approximate horizontal line segment in Fig. 8(e–f). Besides, at the

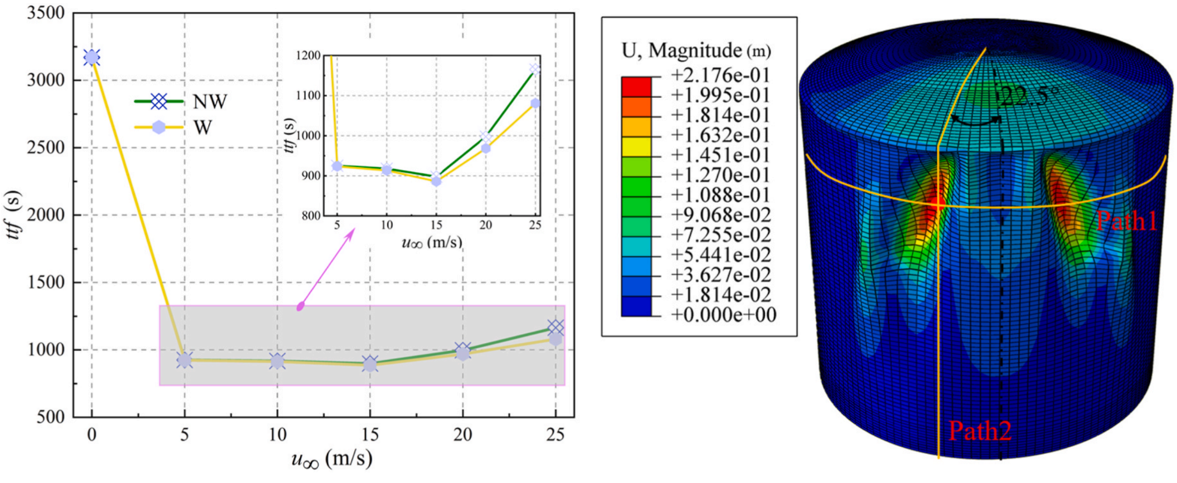

Fig. 7. Fire resistance time at different wind speeds.

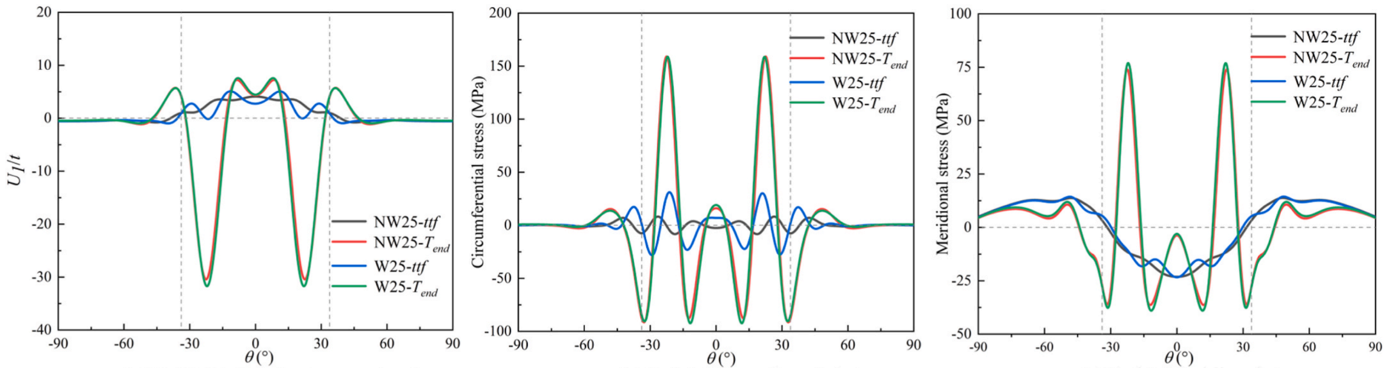

(a) Path1-Radial displacement ratio (b) Path1-Circumferential stress (c) Path1-Meridional stress

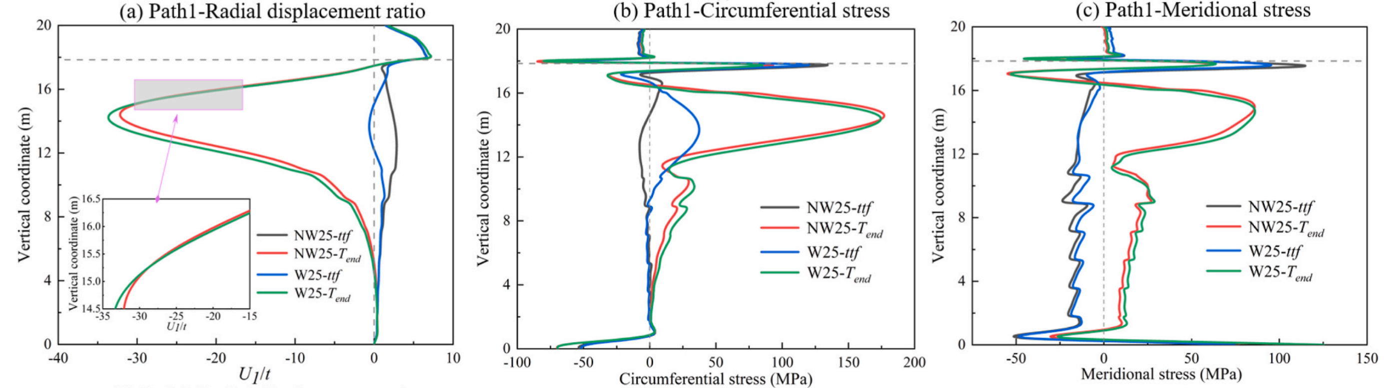

(d) Path2-Radial displacement ratio (e) Path2-Circumferential stress (f) Path2-Meridional stress

Fig. 8. Parameter variations for different paths.

intersection of the tank dome and the tank, the tank dome acts as a restraint to the tank, providing sufficient stiffness so that there is a significant abrupt change in circumferential meridional stresses here.

4.1.2. *Effects of wind speed on thermal post-buckling*

Based on the discussion of paths 1 and 2, it is clear that wind loads can exacerbate the degree of thermal post-buckling effects on the tank. The wall thickness can restrain the deformation of the tank wall to a certain extent. The vertical coordinate U_m/t indicates the deformation magnitude of the tank, expressed as the ratio of the maximum deformation of the tank U_m to the corresponding wall thickness t. P_{w0} indicates the basic wind pressure w_0 on the windward side, NW indicates no wind load, and W indicates wind load.

Fig. 9 shows that the difference in temperature distribution is more pronounced since the wind tilts the flame and the deformation of the tank is more significant with wind. However, the tilting of the flame causes the high-temperature region to be mainly concentrated in the tank dome. The thermal expansion of the tank dome is more significant than that in the absence of wind.

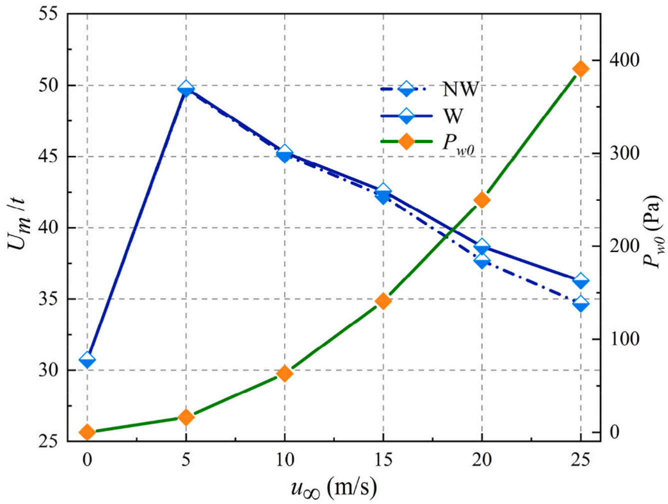

Fig. 9. Deformation of storage tank at different wind speeds.

With the increase of wind speed, the hot area at the tank dome gradually moves backward, the restraint effect of the tank dome on the upper part of the tank wall is reduced, and then the bending moment at the top and bottom of the tank is weakened. As a result, the tank deformation weakens with increasing wind speed. Considering the wind load, the depression deformation of the tank increases for the same wind speed scenario. Although the expansion of the tank dome outward also increases, the wind load has a more significant effect on the disturbance of the tank wall. Therefore, the deformation of the tank subject to thermal post-buckling is the same as the trend when wind load is not considered, except that the degree of deformation produced by the effect of thermal post-buckling of the tank is more severe when wind load is considered.

The above analysis shows that the effect of wind-fire coupling on the thermal post-buckling behavior of storage tanks should be considered in coastal areas or strong wind situations, especially if the pool fire is located at ground level, where the tanks will be fully exposed to the wind loads. When the tank farm is located in a coastal or strong wind-prone area, it is necessary to be alert to the early onset of the thermal post-buckling behavior of the tanks. The excessive reduction of *ttf* and the increase in the deformation are very likely to induce earlier collapse of the tanks, which may lead to a domino effect.

4.2. *Effects of wind angle*

The effect of the wind on the flame may either bring the flame closer to the target tank or move it away from the target tank. Therefore, Taking the wind speed $u_\infty = 20$ m/s and the spacing $d = 20$ m, the thermal buckling under different wind angles is investigated. The temperature distribution and deformation pattern of the target tank for some of the wind angle takes are shown in Fig. 10.

The high-temperature region of the flame shifts from the tank to the tank dome as the γ decreases and the temperature changes from an asymmetric to a symmetric distribution. The rapid increase in T_H means an increase in both the overall temperature and the possibility of thermal post-buckling.

When $\gamma \geq 60$ °C, the tank does not undergo thermal post-buckling, only thermal expansion. Accompanied by the reduction of γ after the target tank undergoes thermal post-buckling, the deformation style changes due to the change in the temperature field distribution but the region covered by the concave deformation expands to some extent.

Fig. 11 shows the variation of parameters related to thermal post-buckling after the change of wind angle. T_L and *ttf* are not recorded for the interval of wind angle where no thermal post-buckling phenomenon occurred ($\gamma \geq 60°$). In the interval of the value of the wind angle γ where the thermal post-buckling of the target tank occurs, the wind angle γ is negatively correlated with the critical buckling temperature T_L, and positively with e *ttf* and the amplitude of buckling (U_m/t).

When the tank undergoes thermal post-buckling behavior, the stability of the structure is reduced and the overall deformation amplitude is intensified due to the abrupt change in geometry. As shown in Fig. 11 (b), the wind angle γ is negatively correlated with the deformation amplitude (U_m/t) of the storage tank during the pre-thermal buckling stage ($60° \leq \gamma \leq 90°$) of the target tank; however, the wind angle γ is positively correlated with the deformation amplitude when the thermal post-buckling phenomenon occurs. For the target tank located in the non-downwind location, although the overall heating rate is reduced, it is also necessary to prevent the appearance of the thermal post-buckling phenomenon to avoid non-linear deformation of the target tank.

4.3. Effects of tank height

Oil storage tanks always consist of different storage tanks with different diameters, heights, and fuels. The height of the tank top fire depends on the height of the storage tanks. As a result, it is needed to consider the role of tank height in the failure of tanks exposed to fire. The wind speed $u_\infty = 20$ m/s and spacing $d = 20$ m is taken as the windy scenario (denoted by W20 in the subsequent illustrations). The wind speed $u_\infty = 0$ m/s and spacing $d = 20$ m are taken as the windless scenario (denoted by W0 in the subsequent illustrations). The thermal buckling behavior of the target tanks in different source tank heights and scenarios is explored.

Fig. 12 presents the temperature distribution and deformation style of the target tank at different source tank heights and in the scene. As the height of the source tank increases, the T_H gradually decreases and the temperature field is always symmetrically distributed. Besides, due to the change in the temperature field distribution, there is a difference in the degree of thermal expansion in each region of the target tank and a change in the deformation pattern.

Considering that there is an interference between the solid flame model and the target tank when the value of the source tank height in the windy scenario is small, the values of the source tank height in different scenarios are not identical. In the thermal buckling process, when the height of the source tank changes, the parameters related to the thermal post-buckling of the target tank in different scenarios are shown in Fig. 13. Due to the increase in the height of the flame position, the distance between the target tank and the flame increases, and the non-uniform thermal expansion rate of the tank decreases. T_H and T_L show a decreasing trend while *ttf* shows an increasing trend, indicating that the thermal post-buckling is delayed, the structural stability of the tank is maintained for a longer time, and U_m/t decreases. Besides, the presence of wind significantly increases the rate of warming, the rate of thermal expansion in each region of the target tank increases, and the

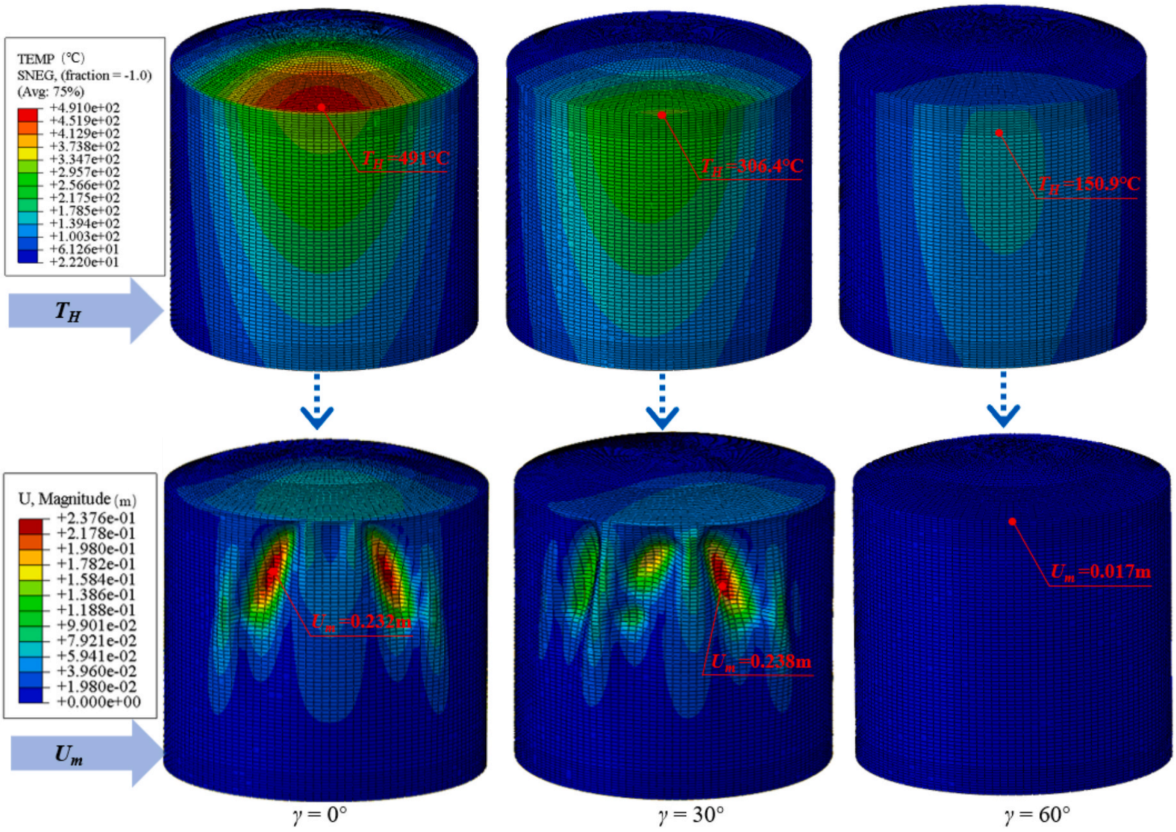

Fig. 10. Temperature and deformation distribution under different wind angles.

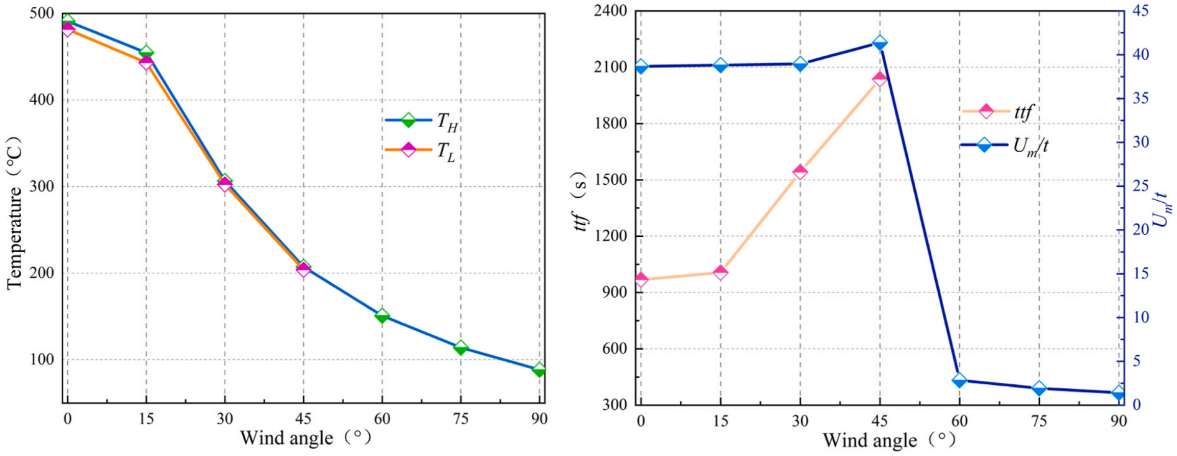

(a) Comparison of temperature parameters (b) Comparison of *ttf* and deformation

Fig. 11. Parameter changes in thermal post-buckling under different wind angles.

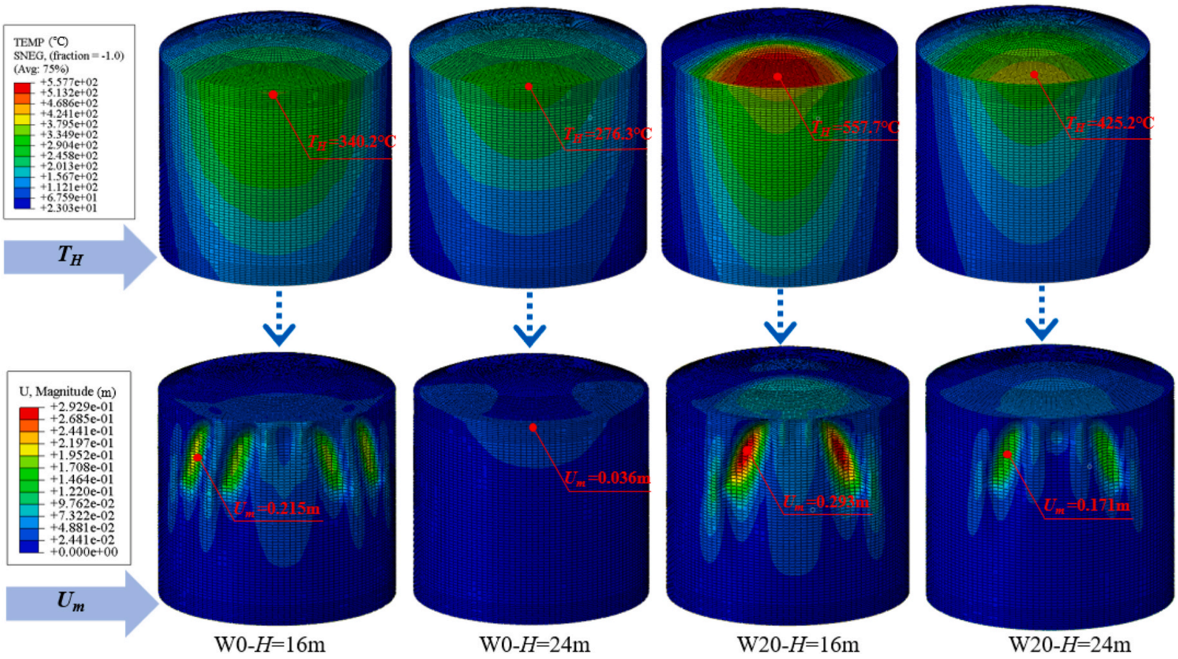

Fig. 12. Temperature and deformation distribution under different flame heights.

degree of non-uniform thermal expansion is intensified, so the T_L shows an opposite trend in the two scenarios.

At the same source tank height, *ttf* in the windy scenario appears to be significantly lower while U_m/t is significantly higher, i.e., the magnitude of tank deformation increased. In addition, in the sample with $H = 24$ m, the thermal post-buckling of the target tank occurs only in the windy scenario, but not in the windless scenario. Therefore, when the tank is subjected to wind-fire coupling, it is more prone to thermal post-buckling.

4.4. Effects of tank diameter

In the early stages of tank design, the layout is varied and idealized but subject to the needs of the actual production and site size constraints, and the diameter of adjacent tanks may not be consistent. The pool fire diameter is positively correlated with the source tank diameter. When the source tank diameter becomes larger, the target tank receives more heat per unit time and the temperature field distribution also changes. This sub-section explores the effect of source tank diameter on the thermal buckling behavior of storage tanks in different scenarios.

As shown in Fig. 14, with increasing the diameter of the source tank, the heating rate becomes larger, the T_H rises, and the high-temperature region of the target tank expands to both sides. In different scenarios, the temperature field is symmetrically distributed, but the distribution style of the high-temperature region is not the same. Besides, during thermal buckling, when the diameter of the source tank changes, the temperature field distribution of the target tank changes, and its deformation style is different.

The parameters associated with thermal post-buckling are shown in Fig. 15. When the source tank diameter D increases, the non-uniform thermal expansion rate of the target tank accelerates, and thermal post-buckling is more likely to occur, corresponding to a decrease in *ttf*. Although *ttf* is negatively correlated with the source tank diameter, due to the significant increase in the heating rate, T_L and T_H still tend to

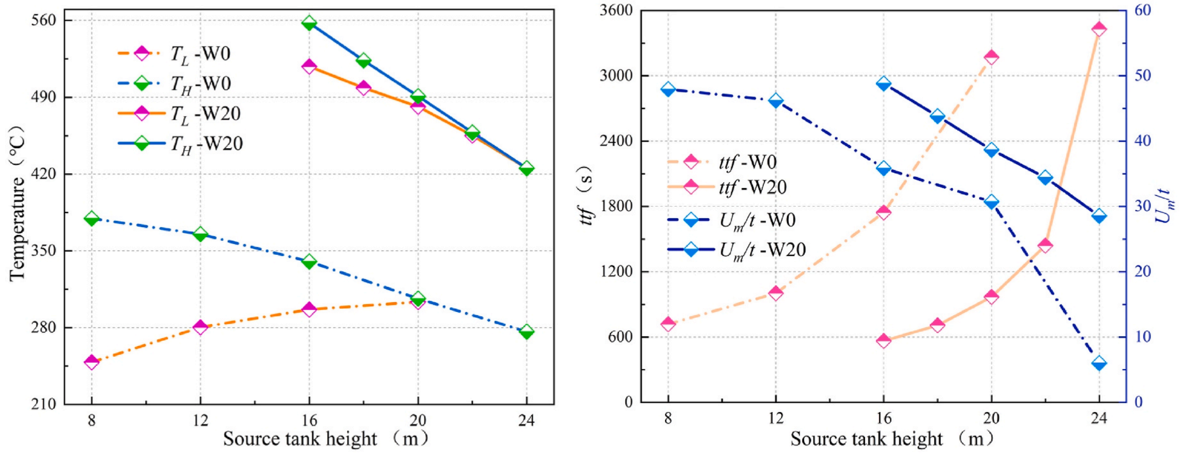

(a) Comparison of temperature parameters (b) Comparison of ttf and deformation

Fig. 13. Parameter changes in thermal post-buckling under different flame heights.

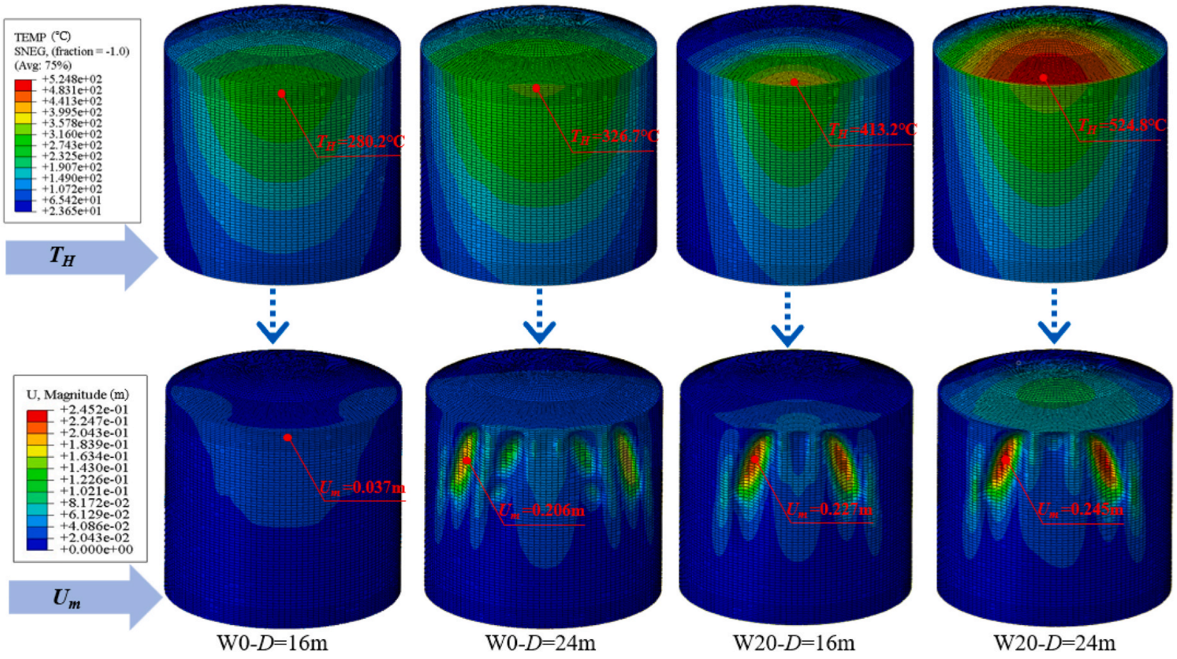

Fig. 14. Temperature and deformation distribution under different tank diameters.

increase, and both are positively correlated with the source tank diameter.

The results show that when the thermal post-buckling stage occurs, the deformation amplitude increases with increasing the source tank diameter. Comparing the samples taken with $D = 16$ m, the target tanks only undergo thermal post-buckling in the windy scenario; in the rest of the pool fire diameter samples taken in the windy scenario, the deformation amplitude of the tanks increases significantly, and the *ttf* decreases significantly. Pool fires caused by large storage tanks should be extinguished first to prevent thermal post-buckling of the surrounding tanks and to avoid induced collapses.

5. Conclusions

This paper researches the coupled effects of thermal loads and wind loads on the buckling behavior of storage tanks via a numerical simulation. This study can be used to determine the time to failure of tanks exposed to fire, avoiding underestimating the risk of domino effects and supporting the inherent design and safety barrier management of storage tank areas. According to this study, the following conclusions are drawn:

(1) Thermal post-buckling plays a pivotal role in the failure of storage tanks exposed to coupled effects of fire and wind loads. In the thermal post-buckling stage, the weak region of the tank appears nonlinear deformation, geometry changes abruptly, and the stress shows fluctuating changes, resulting in the reduction of the structural stability and the weakening of the load-carrying capacity.
(2) At the downwind location, under the positive pressure of the wind, the thermal expansion of the frontal high-temperature region of the storage tank is weakened, and inward concave deformation occurs, contributing to the premature thermal post-buckling of the storage tank. The tank deformation increases

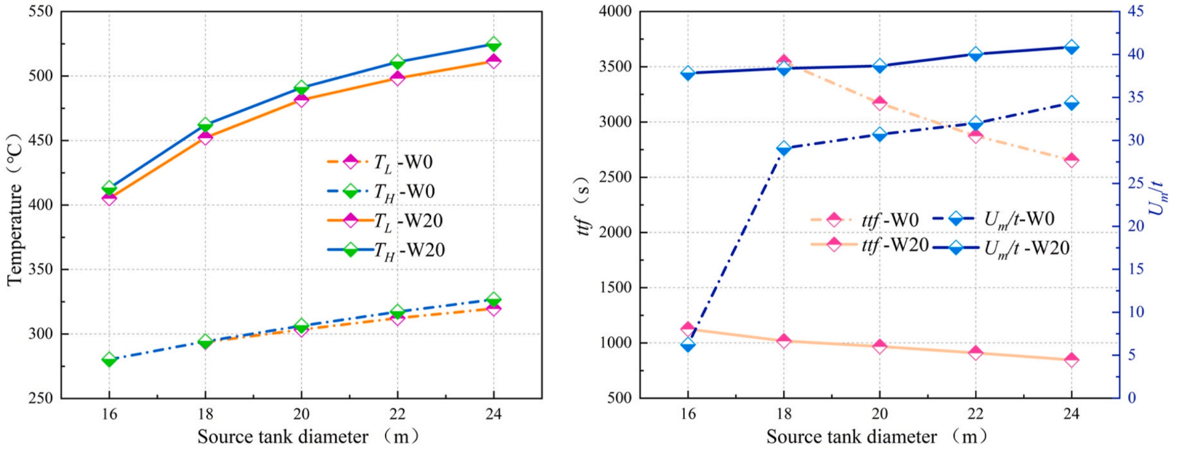

(a) Comparison of temperature parameters (b) Comparison of *ttf* and deformation

Fig. 15. Parameter changes in thermal post-buckling under different tank diameters.

when wind loads are applied. Tanks are more likely to show post-thermal buckling in the windy scenario and the *ttf* is greatly reduced and the deformation is intensified.

(3) Risk assessment and loss prevention in tank farms must take into account the effects of the coupled effects of fire and wind loads to avoid potentially catastrophic consequences, especially for tank storage areas that are susceptible to strong winds or coastal areas.

(4) The thermal buckling studied in this study is triggered by the non-uniform thermal expansion and non-uniform wind loads of thin-walled structures. In the future, this study can be extended to model the thermal buckling of other thin-walled vessels. Besides, the performance of tanks with fireproof coatings and the scenarios with multiple tanks can also be investigated by applying the developed numerical model. As a result, the most critical tanks in the domino effect chain can be identified for guiding the inherent design of storage tank areas and safety barrier allocation.

Credit author statement

Chao Chen: Writing-Original draft, Methodology, Supervision; **Hang Chen:** Writing-Original draft, Programming; **Mo Li:** Writing-Reviewing and Editing, Conceptualization; **Shenbin Xiao:** revising the manuscript, Programming; **Chanjun Li:** Supervision, Resources; **Ming Yang:** Visualization, Writing- Reviewing and Editing; **Genserik Reniers**: Supervision, Writing- Reviewing and Editing.

Declaration of competing interest

The authors declare that they have no known competing financial interests or personal relationships that could have appeared to influence the work reported in this paper.

Data availability

Data will be made available on request.

Acknowledgments

This study was supported by the Sichuan Province Science and Technology Support Program (Grant No. 2022NSFC0235, 2023YFS0412). We also appreciate the editor and anonymous reviewers.

References

ACI-ASCE Committee 334, 1976. Reinforced Concrete Cooling Tower Shells: Practice and Commentary. American Concrete Institute.

API, 2007. Welded Steel Tanks for Oil Storage. American Petroleum Institute, Washington D. C.

Batista-Abreu, J.C., Godoy, L.A., 2013. Thermal buckling behavior of open cylindrical oil storage tanks under fire. J. Perform. Constr. Facil. 27, 89–97.

Beyler, C.L., 2016. Fire Hazard Calculations for Large, Open Hydrocarbon Fires, SFPE Handbook of Fire Protection Engineering. Springer, pp. 2591–2663.

Chen, C., Reniers, G., Khakzad, N., 2020. A thorough classification and discussion of approaches for modeling and managing domino effects in the process industries. Saf. Sci. 125.

Chen, C., Reniers, G., Khakzad, N., 2021. A dynamic multi-agent approach for modeling the evolution of multi-hazard accident scenarios in chemical plants. Reliab. Eng. Sys. Saf. 207.

Darbra, R.M., Palacios, A., Casal, J., 2010. Domino effect in chemical accidents: main features and accident sequences. J. Hazard Mater. 183, 565–573.

Ding, L., Khan, F., Guo, X., Ji, J., 2021. A novel approach to reduce fire-induced domino effect risk by leveraging loading/unloading demands in chemical industrial parks. Process Saf. Environ. Protect. 146, 610–619.

Dong, D., Yuan, F., 2000. Practical Manual for Pressure Vessels and Chemical Equipment.

Dong, X., Ding, X., Li, G., Lewis, G.P., 2020. Stiffener layout optimization of plate and shell structures for buckling problem by adaptive growth method. Struct. Multidiscip. Optim. 61, 301–318.

Drysdale, D., 2011. An Introduction to Fire Dynamics. John wiley & sons.

Espinosa, S.N., Jaca, R.C., Godoy, L.A., 2019. Thermal effects of fire on a nearby fuel storage tank. J. Loss Prev. Process. Ind. 62.

GB50009, 2012. Code of loads for the design of building structures. Ministry of Housing and Urban-Rural Development of the People's Republic of China.

GB50341, 2014. Code for Design of Vertical Cylindrical Welded Steel Oil Tanks. Ministry of Housing and Urban-Rural Development of the People's Republic of China.

GB/T 20368, 2006. Liquefied natural gas (LNG) production, storage, and shipping. Standards Press of China.

Godoy, L.A., 2007. Performance of storage tanks in oil facilities damaged by Hurricanes Katrina and Rita. J. Perform. Constr. Facil. 21, 441–449.

Godoy, L.A., 2016. Buckling of vertical oil storage steel tanks: review of static buckling studies. Thin-Walled Struct. 103, 1–21.

Godoy, L.A., Batista-Abreu, J.C., 2012. Buckling of fixed-roof aboveground oil storage tanks under heat induced by an external fire. Thin-Walled Struct. 52, 90–101.

He, Z., Chen, C., Weng, W., 2022. Multi-hazard risk assessment in process industries: State-of-the-Art. J. Loss Prevent. Process Ind. 76, 104672.

Hu, K., 2016. Numerical Simulation of Explosion Loading and Dynamic Response of Steel Tanks. Zhejiang University. Zhejiang University, Hangzhou.

Hurley, M.J., Gottuk, D.T., Hall Jr., J.R., Harada, K., Kuligowski, E.D., Puchovsky, M., Watts Jr., J.M., Wieczorek, C.J., 2015. SFPE Handbook of Fire Protection Engineering. Springer.

Jaca, R.C., Godoy, L.A., Calabró, H.D., Espinosa, S.N., 2021. Thermal post-buckling behavior of oil storage tanks under a nearby fire. Int. J. Pres. Ves. Pip. 189.

Jiang, D., Pan, X.-H., Hua, M., Mébarki, A., Jiang, J.-C., 2019. Assessment of tanks vulnerability and domino effect analysis in chemical storage plants. J. Loss Prev. Process. Ind. 60, 174–182.

Jin, X., Zhao, J., 2012. Development of the design code for building structures in China. Struct. Eng. Int. 22, 195–201.

Lan, M., Gardoni, P., Qin, R., Zhang, X., Zhu, J., Lo, S., 2022. Modeling NaTech-related domino effects in process clusters: a network-based approach. Reliab. Eng. Syst. Saf. 221.

Landucci, G., Gubinelli, G., Antonioni, G., Cozzani, V., 2009. The assessment of the damage probability of storage tanks in domino events triggered by fire. Accid. Anal. Prev. 41, 1206–1215.
Li, X., Chen, G., Amyotte, P., Alauddin, M., Khan, F., 2023a. Modeling and analysis of domino effect in petrochemical storage tank farms under the synergistic effect of explosion and fire. Process Saf. Environ. Protect. 176, 706–715.
Li, X., Chen, G., Amyotte, P., Khan, F., Alauddin, M., 2023b. Vulnerability assessment of storage tanks exposed to simultaneous fire and explosion hazards. Reliab. Eng. Syst. Saf. 230.
Li, Y., Jiang, J., Yu, Y., Wang, Z., Xing, Z., Zhang, Q., 2021. Fire resistance of a vertical oil tank exposed to pool-fire heat radiation after high-velocity projectile impact. Process Saf. Environ. Protect. 156, 231–243.
Li, Y., Jiang, J., Zhang, Q., Yu, Y., Wang, Z., Liu, H., Shu, C.-M., 2019. Static and dynamic flame model effects on thermal buckling: fixed-roof tanks adjacent to an ethanol pool-fire. Process Saf. Environ. Protect. 127, 23–35.
Lin, W., Zhang, N., Gu, A., 2010. LNG (liquefied natural gas): a necessary part in China's future energy infrastructure. Energy 35, 4383–4391.
Liu, Y., 2011. Thermal Buckling of Metal Oil Tanks Subject to an Adjacent Fire. University of Edinburgh, Scotland.
Malik, A.A., Nasif, M.S., Arshad, U., Mokhtar, A.A., Tohir, M.Z.M., Al-Waked, R., 2023. Predictive modelling of wind-influenced dynamic fire spread probability in tank farm due to domino effect by integrating numerical simulation with ANN. Fire 6.
Mansour, K.A., 2012. Fires in Large Atmospheric Storage Tanks and Their Effect on Adjacent Tanks. Loughborough University.
Maraveas, C., Balokas, G.A., Tsavdaridis, K.D., 2015. Numerical evaluation on shell buckling of empty thin-walled steel tanks under wind load according to current American and European design codes. Thin-Walled Struct. 95, 152–160.
Mudan, K.S., 1984. Thermal radiation hazards from hydrocarbon pool fires. Prog. Energy Combust. Sci. 10, 22.
Muñoz, M., Planas, E., Ferrero, F., Casal, J., 2007. Predicting the emissive power of hydrocarbon pool fires. J. Hazard Mater. 144, 725–729.
Necci, A., Cozzani, V., Spadoni, G., Khan, F., 2015. Assessment of domino effect: state of the art and research Needs. Reliab. Eng. Syst. Saf. 143, 3–18.
Paltrinieri, N., Landucci, G., Molag, M., Bonvicini, S., Spadoni, G., Cozzani, V., 2009. Risk reduction in road and rail LPG transportation by passive fire protection. J. Hazard Mater. 167, 332–344.
Pantousa, D., 2018. Numerical study on thermal buckling of empty thin-walled steel tanks under multiple pool-fire scenarios. Thin-Walled Struct. 131, 577–594.
Pantousa, D., Godoy, L.A., 2019. On the mechanics of thermal buckling of oil storage tanks. Thin-Walled Struct. 145, 106432.
Pantousa, D., Tzaros, K., Kefaki, M.-A., 2018. Thermal buckling behaviour of unstiffened and stiffened fixed-roof tanks under non-uniform heating. J. Constr. Steel Res. 143, 162–179.
Portela, G., Godoy, L., 2005a. Wind pressures and buckling of cylindrical steel tanks with a conical roof. J. Constr. Steel Res. 61, 786–807.
Portela, G., Godoy, L., 2005b. Wind pressures and buckling of cylindrical steel tanks with a dome roof. J. Constr. Steel Res. 61, 808–824.
Rebec, A., Plešec, P., Kolšek, J., 2014. Pool fire accident in an aboveground LFO tank storage: thermal analysis. Fire Saf. J. 67, 135–150.
Reniers, G., Cozzani, V., 2013. Domino Effects in the Process Industries, Modeling, Prevention and Managing. Elsevier, Amsterdam, The Netherlands.
Rew, P., Hulbert, W., Deaves, D., 1997. Modelling of thermal radiation from external hydrocarbon pool fires. Process Saf. Environ. Protect. 75, 81–89.
Rish, R.F., Fourier, 1967. Forces in cylindrical chimneys due to wind. Proc. Inst. Civ. Eng. 36, 791–803.
Santos, F.d.S., Landesmann, A., 2014. Thermal performance-based analysis of minimum safe distances between fuel storage tanks exposed to fire. Fire Saf. J. 69, 57–68.
Thomas, P., 1963. The Size of Flames from Natural Fires, Symposium (International) on Combustion. Citeseer, pp. 844–859.
Uematsu, Y., Yamaguchi, T., Yasunaga, J., 2018. Effects of wind girders on the buckling of open-topped storage tanks under quasi-static wind loading. Thin-Walled Struct. 124, 1–12.
Zhang, M., Zheng, F., Chen, F., Pan, W., Mo, S., 2019. Propagation probability of domino effect based on analysis of accident chain in storage tank area. J. Loss Prev. Process. Ind. 62.
Zhao, Y., Lin, Y., 2014. Buckling of cylindrical open-topped steel tanks under wind load. Thin-Walled Struct. 79, 83–94.

Further reading

Stathopoulos, T., Alrawashdeh, H., 2020. Wind loads on buildings: a code of practice perspective. J. Wind Eng. Ind. Aerod. 206, 104338.

Glossary

D: the diameter of the source tank (m)
D_f: the flame diameter (m)
D'_f: the long axis of the elliptical cross-section of the flame (m)
H: the height of the source tank (m)
L_f: the flame length (m)
L^*: the characteristic length (m)
F_r: the Froude number
F_D: the artificial damping force
L_1: the length of the bright flame part of the flame (m)
m^*: the non-dimensional mass burning rate of the fuel
m_b: the mass combustion rate of the fuel (kg/m^{2}s)
k_β: the fuel experience coefficient
g: the acceleration of gravity (m/s^2)
d: the distance between the two tanks (m)
Re: the Reynolds number
w_k: the wind pressure amplitude (Pa)
M^*: the artificial mass matrix of unit density
N_u: the Nusselt number
c_i: the Fourier coefficient
P_r: the Prandtl number
U_m: the maximum deformation of the tank (mm)
U_1: the radial displacement (mm)
Z: the height from the ground (m)
K_a: he thermal conductivity of air (W/m·K)

Greek symbols

θ: the angle along the circumferential direction (°)
φ: the flame tilt angle (°)
γ: the wind angle (°)
ε: the emissivity of the flame
σ: the Stefan-Boltzmann constant
τ: the atmospheric transmittance
λ: the load amplification factor
k: thermal conductivity (W/m/K)
α: coefficient of thermal expansion
N_c: the number of carbon atoms in the fuel
N_H: the number of hydrogen atoms in the fuel
T_{fe}: the equivalent temperature of the flame surface (°C)
T: Temperatures (°C)
T_H: the maximum temperature (°C)
T_L: the critical buckling temperature (°C)
T_{end}: the 3600th s of the warming process
E_{av}: the average emitted power (kW/m^2)
$E_{av\text{-}max}$: the average emission power of bright flames (kW/m^2)
E_{max}: the maximum real firing power of the bright flame (kW/m^2)
E_{soot}: the maximum firing power of the dark flame (kW/m^2)
P_c: the circumferential wind pressure (Pa)
P: the total external load
Q: the internal force
ttf: the refractory time (s)
w_0: the basic wind pressure (Pa)
c_p: the constant pressure specific heat (J/kg/K)
E: modulus of elasticity (GPa)
c: the damping ratio
t: the tank wall thickness (mm)
P_{w0}: the basic wind pressure on the windward side (Pa)
W_c: the wind class
$\overline{h}_c$: the average convective heat transfer coefficient (W/m^2·K)
μ_z: the wind pressure height variation coefficient
ρ: the air density (kg/m^3)
u^*: the dimensionless wind speed
u_∞: the free field wind speed (m/s)
β_z: the wind vibration coefficient
μ_s: the wind load shape coefficient
υ: the velocity vector of the node
ν: the kinematic viscosity of air (m^2/s)
μ: Poisson's ratio